RESEARCH ARTICLE

Incomplete fluid–structure coupling mechanism of a flexible membrane wing

Xi He[1] · Jinjun Wang[1]

Abstract

The effect of angles of attack (α) on the fluid–structure coupling of a flexible membrane wing is investigated experimentally at $Re = 6 \times 10^4$. Membrane deformations and the surrounding flow fields are measured synchronously by two-dimensional time-resolved particle image velocimetry (2D-TRPIV). Results show that, for $12 \leq \alpha \leq 16°$, the vertical velocities over the membrane are coupled with the membrane vibration, but the streamwise velocities present lower dominant frequencies, which means the susceptibility of the flow in vertical and streamwise directions is different. As a result, the dominant frequencies of the instantaneous flows are different from and lower than the membrane, suggesting that the flow and the membrane are incompletely coupled. Then, the incomplete fluid–structure coupling mechanism is clearly revealed by the colored virtual dye visualization as well as the instantaneous pressure gradients. The periodically alternating adverse and favorable pressure gradients near the leading edge lead to the unsteady flow separation and reattachment, resulting in periodic presence and absence of the trailing-edge reverse flow in streamwise direction. Consequently, the intermittent fluid–fluid interaction between the leading-edge flow and the trailing-edge reverse flow causes the incomplete fluid–structure coupling.

Graphical abstract
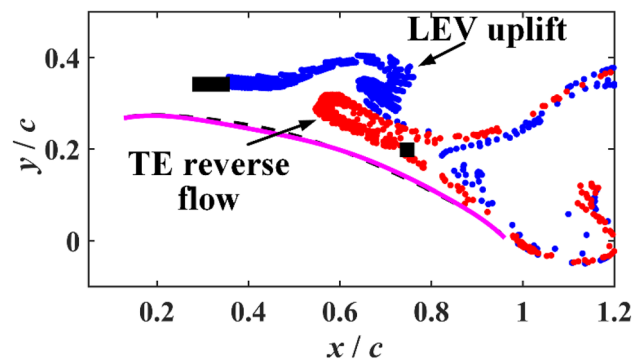
1 Introduction

Due to the unique advantages on stall delay and circumstance adaptability, flexible membrane wings have practical significance for the development of advanced microair vehicles (MAVs). When aerodynamic loads are applied, the flexible surface can deform adaptively and thereby influence the aerodynamic performance of the wing.

Commonly, simplified single-layer flexible membrane wings were designed and investigated for fundamental research of fluid–structure interaction (FSI). The membrane motion could be mainly divided into two states at $\alpha > 0°$ with various lift-enhancement regularities: deformed steady state (DSS) at pre-stall and dynamic balance state (DBS) at around stall and post-stall (Li et al. 2021; He et al. 2022). In the DSS region, the membrane wing bent under aerodynamic loads and maintained at the mean camber with negligibly

✉ Jinjun Wang
  jjwang@buaa.edu.cn

1 Fluid Mechanics Key Laboratory of Education Ministry,
   Beijing University of Aeronautics and Astronautics,
   Beijing 100191, China

small vibration. The increased mean camber could result in lift enhancement, which conforms to the basic theory of aerodynamics. In the DBS region, the membrane wing began to vibrate coherently around the mean camber while interacting with the surrounding flow, presenting various vibration modes related to the natural frequencies of the membrane (Song et al. 2008; Gordnier 2009; Rojratsirikul et al. 2009, 2010; He and Wang 2020). Except for the effect of mean camber, the unsteady vibration could also increase the lift by enhancing momentum mixing and suppressing flow separation (Rojratsirikul et al. 2009; He et al. 2022).

Generally, the mechanism of the unsteady flow-induced vibration is the frequency lock-in phenomenon between vortex shedding and membrane vibration. Relevant numerical simulations (Gordnier 2009; Tiomkin et al. 2011; Li et al. 2021) and wind tunnel experiments (Song et al. 2008; Tregidgo et al. 2013; Bleischwitz et al. 2017; Waldman and Breuer 2017; He and Wang 2020) have found the close-coupling relationship between dynamic vortex shedding and membrane response at different operating conditions. The vortex shedding frequency in the shear layer or wake region was related to the membrane natural frequencies and its harmonics and finally selected a certain vibration mode and vortex shedding mode (Li et al. 2022). Huang et al. (2021) found two kinds of fluid–structure interaction with numerical simulation, i.e., the membrane response was mainly driven by the natural frequency of structure for $\alpha = 4° \sim 12°$ and by the evolution of leading- and trailing-edge vortices for $\alpha = 16° \sim 24°$, respectively. Xia et al. (2023) further introduced the aerodynamic stiffness effect and the added-mass effect into the natural frequency model of the membrane. By comparing the corrected natural frequency and the vortex shedding one, they found the mode transition of the membrane was caused by the transition of fluid–structure coupling state. Bleischwitz et al. (2017) reported that membrane motions were coupled with flow separation at either high angle of attack or ground effect environment, and they confirmed the ability of flexible membrane wings to modify the frequency of vortex shedding by the vibration eigenfrequency of the membrane. Tiomkin et al. (2011) studied the effect of angle of attack on a membrane wing in viscous laminar flow and indicated the membrane shape corresponded with oscillations at the vortex shedding frequency. In this sense, the membrane and the flow in the literature above were completely coupled with identical dominant frequencies.

However, in addition to the complete fluid–structure coupling, we have found that the flow over the membrane wing had a lower dominant frequency than the membrane-fluid lock-in frequency, which was interpreted as the result of fluid–fluid interaction between the flows from leading edge (LE) and trailing edge (TE) (He and Wang 2020). This phenomenon was also reported by the subsequent experiment

of Rodríguez-López et al. (2021). However, only the effect of Reynolds number was investigated in our previous study. The influences of other important parameters need to be further explored. Accordingly, the current study focuses on the effect of angles of attack on this incomplete coupling phenomenon, aiming to find out more comprehensive characteristics of the fluid–structure interaction of membrane wing as well as the fluid–fluid interaction between flows from LE and TE. In this paper, the flow fields and membrane deformations were captured simultaneously by time-resolved particle image velocimetry (TRPIV). $Re = 6 \times 10^4$ was selected based on the results of He and Wang (2020). The full text is divided into the following parts: introduction, experimental methods, membrane kinematics, fluid–structure interaction and conclusions.

2 Experimental methods

The present experiment was carried out in the low-speed, open-loop and closed-jet D6 wind tunnel at the Beijing University of Aeronautics and Astronautics (BUAA). The test section of the wind tunnel has a cross section of 430 mm (width) × 500 mm (height) with the free stream turbulent intensity Tu of about 0.3% at the current operating conditions.

2.1 Model design

The current model was a simplified LE- and TE-supported membrane wing, whose structure is illustrated in Fig. 1. A sheet of membrane was wrapped around 3-mm round steel LE and TE to form a complete membrane wing. To minimize the leading-edge separation, the membrane was able to freely rotate about the LE and TE at a given α. The membrane was made of a highly transparent thermoplastic polyurethanes (TPU) sheet with a thickness of $t_m = 0.2$ mm,
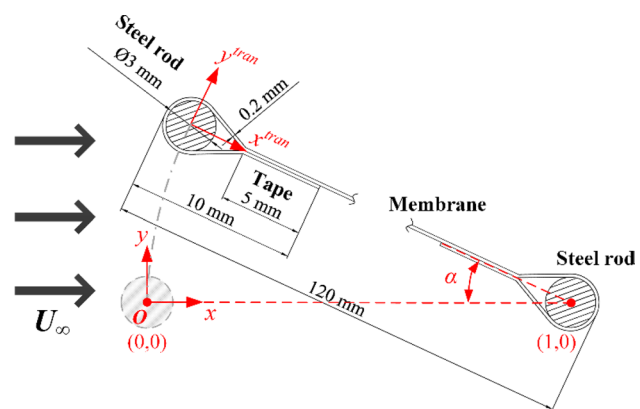

Fig. 1 Membrane wing model

Young's modulus of $E = 31.2$ MPa and density of $\rho_m = 1.1$ g/cm^3. The angle of attack is also shown in Fig. 1.

The coordinate system of the flow fields (x–y plane) is defined in Fig. 1. The x–y plane is a wing-normal plane with the x-axis parallel to the free stream. As illustrated in Fig. 1, the origin O of x–y plane is located at the LE when $\alpha = 0°$. The membrane instantaneous locations are then translated to ensure the nondimensional coordinates of the TE to be (1, 0) at any α. In addition, another coordinate system for analyses of membrane kinematics (x^{tran}–y^{tran} plane) is also defined in Fig. 1. It is obtained by rotation of x–y plane, and the new origin is located at the LE at any α.

The experimental setup is shown in Fig. 2. The membrane wing model was horizontally mounted in the test section through the LE and TE supports and two circular endplates. Both the LE and TE stretched across the whole span between the endplates with their ends fixed to the endplates. There was a narrow spanwise gap (~5 mm) between the membrane and the endplates. The endplates could eliminate the boundary layer effect by installing the model outside the boundary layer of the wind tunnel walls. The wing had a span of 380 mm and chord length of $c = 120$ mm, so the aspect ratio was 3.17 and larger than 3.0, which could ensure the quasi-2D of the flow at the mid-span of the wing (Mizoguchi and Itoh 2013; Bleischwitz et al. 2015). The free stream velocity U_∞ was 7.5 m/s, so the Reynolds number based on c was 6×10^4. To investigate the effect of angles of attack on the membrane wing, the membrane deformations and the flow fields were measured at $\alpha = 8°$, $12°$, $14°$, $16°$ and $20°$, which covered the range from pre-stall to post-stall according to He et al. (2022). The angles of attack could be adjusted by the holes on the endplate. The blockage ratio of the wing model was around 7.2% at $\alpha = 20°$, and the additional blockage ratio of the endplates was around 1.3%. Therefore, the total blockage ratio was approximately 8.5%.
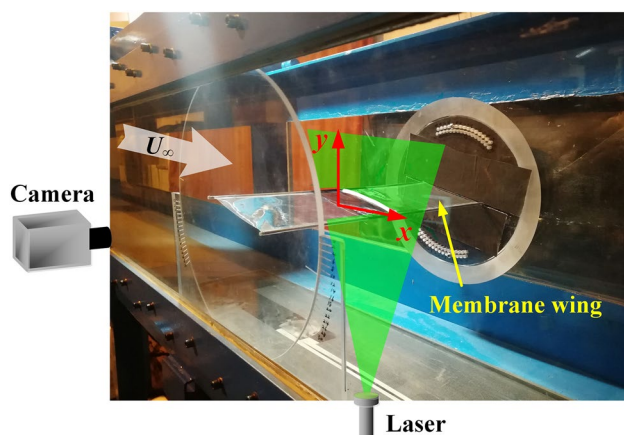

Fig. 2 Experimental setup. The white curve on the membrane surface is an example for deformation measurement

2.2 Measurements

As displayed in Fig. 2, the 2D-TRPIV was conducted in x–y plane at the mid-span of the wing model. Glycerol–water mixture droplets with a mean diameter of about 1 μm were generated and seeded by an AG 1500 W fog machine as the tracer particles. The desired plane was illuminated by a Beamtech Vlite-Hi-527–30 high-speed dual-pulsed laser with a minimum energy of 30 mJ/pulse at 1 kHz frame rate. The laser pulse duration at the full-width-half-maximum (FWHM) location was less than 200 ns. The thickness of the laser sheet was approximately 1.5 mm. The laser sheet was able to illuminate both the upper and lower sides of the wing because of the high transparency of the membrane. Therefore, the global flow field around the wing as well as the instantaneous membrane deformations could be captured. A Photron Fastcam SA2/86 K-M3 high-speed CMOS camera was placed normal to the x–y plane to capture image pairs. The laser and the camera were synchronized by a MicroVec Micropulse-725 synchronizer. The uncertainty of the synchronizer was less than 0.25 ns, which was high enough for accurately synchronous control. The sampling frequency of PIV image pairs was set to 1 kHz, and 1.9×10^4 image pairs (namely 1.9×10^4 snapshots of velocity fields) with the sampling duration of 19 s could be captured at one time. The spatial resolution of the camera was tailored to 768×672 pixels to realize high-speed double-exposure function. The size of the field of view (FOV) was 144×126 mm^2, so the magnification was $144/768 \approx 0.19$ mm/pixel. The time delay between one image pair was 250 μs. The recorded 12-bit raw particle images were processed based on the multi-pass iterative Lucas–Kanade (MILK) algorithm accelerated by graphic processing units (GPUs) to obtain original velocity fields (Champagnat et al. 2011; Pan et al. 2015). The interrogation window size was set to 32×32 pixels^2 with a 75% overlap. Therefore, the physical grid resolution of the PIV data was $32 \times (144/768) = 6$ mm.

The uncertainty of the particle displacement in PIV measurements was less than 0.1 pixel by using the sub-pixel interpolation and multigrid iteration with window deformation (He et al. 2016). The maximum particle displacements in all cases were in the range of 12 ~ 16 pixels. Thus, the relative uncertainties of the particle displacements were less than 0.8% ($0.1/12 \approx 0.8\%$). Referring to Qu et al. (2019), the particle velocity u_p in the PIV measurement was

$$u_p = x_p / t_p, \tag{1}$$

where x_p is the physical displacement of particles between one image pair, and $t_p = 250$ μs is the corresponding time delay. The relative uncertainty of u_p originating from both

the uncertainties of x_p and t_p could be estimated by the uncertainty propagation formula (Kline and McClintock 1953):

$$
\begin{aligned}
\frac{\varepsilon(u_p)}{U_\infty} &= \frac{1}{U_\infty} \sqrt{\left(\frac{\partial u_p}{\partial x_p}\right)^2 \varepsilon^2(x_p) + \left(\frac{\partial u_p}{\partial t_p}\right)^2 \varepsilon^2(t_p)} \\
&= \frac{1}{U_\infty} \sqrt{\left(\frac{1}{t_p}\right)^2 \varepsilon^2(x_p) + \left(-\frac{x_p}{t_p^2}\right)^2 \varepsilon^2(t_p)},
\end{aligned}
\tag{2}
$$

where ε denotes the uncertainties. In this study, t_p was determined by the synchronizer with $\varepsilon(t_p) = 0.25$ ns. As mentioned above, the maximum uncertainty of the particle displacement was 0.1 pixel. The corresponding $\varepsilon(x_p)$ was 1.9×10^{-2} mm (0.1 pixel multiplied by the magnification). Thus, the velocity uncertainty relative to the free stream velocity was approximately 1.0%.

The approach of recognizing membrane deformation was elaborated in previous studies (Hu et al. 2020; He and Wang 2020; He et al. 2022). The sampling frequency of deformation measurement was also 1 kHz because the membrane deformations were strictly synchronized with the flow fields. It can provide pixel accuracy of 0.16% c ($0.19/120 \approx 0.16\%$) with a resolution of 0.19 mm/pixel, the same as the magnification of PIV.

2.3 Post-processing methods

2.3.1 Virtual dye visualization

Similar to the dye visualization in real experiments, virtual dye visualization (VDV) visualizes the attracting Lagrangian coherent structures (LCS) in the flow. Virtual tracers are released from a certain location and then convected with the flow, revealing the nearby LCS (Shadden et al. 2006, 2007). The interactions between different flow patterns can be clearly visualized by emitting virtual tracers with different colors (He et al. 2017; Wang and Wang 2021). In the current study, the trajectories of the virtual tracers are calculated from PIV data using the iterative algorithm of the "pseudo-tracing" technique (Jensen et al. 2003; Liu and Katz 2006), which provides acceptable accuracy on the calculation of material accelerations of the virtue tracers.

2.3.2 Pressure gradients calculation

Based on the time-resolved PIV data, the instantaneous pressure gradients ∇p can be obtained by the incompressible Navier–Stokes equation:

$$
\nabla p = -\rho_a \frac{D\mathbf{u}}{Dt} + \mu \nabla^2 \mathbf{u},
\tag{3}
$$

where ρ_a is the air density, $\mathbf{u}$ is the 2D velocity vector, μ is the dynamic viscosity coefficient. In Eq. (3), ∇p is calculated by adding the material derivative term and the viscosity term. The material accelerations have been obtained by "pseudo-tracing" technique, and the viscosity term can be directly obtained from PIV data by adopting central difference scheme.

3 Membrane kinematics

The superpositions of membrane patterns at different angles of attack are displayed in Fig. 3. The black and red curves represent the mean $\langle y^{tran}(x^{tran}) \rangle$ and instantaneous $y^{tran}(x^{tran}, t)$ membrane deformations along the chord, respectively. Based on Fig. 3, the variation of the mean camber and the vibration amplitude A^* of the membrane wing are shown in Fig. 4. A^* is the standard deviations of the membrane displacements along y^{tran} direction. It is shown in the figures that both the mean camber and the vibration
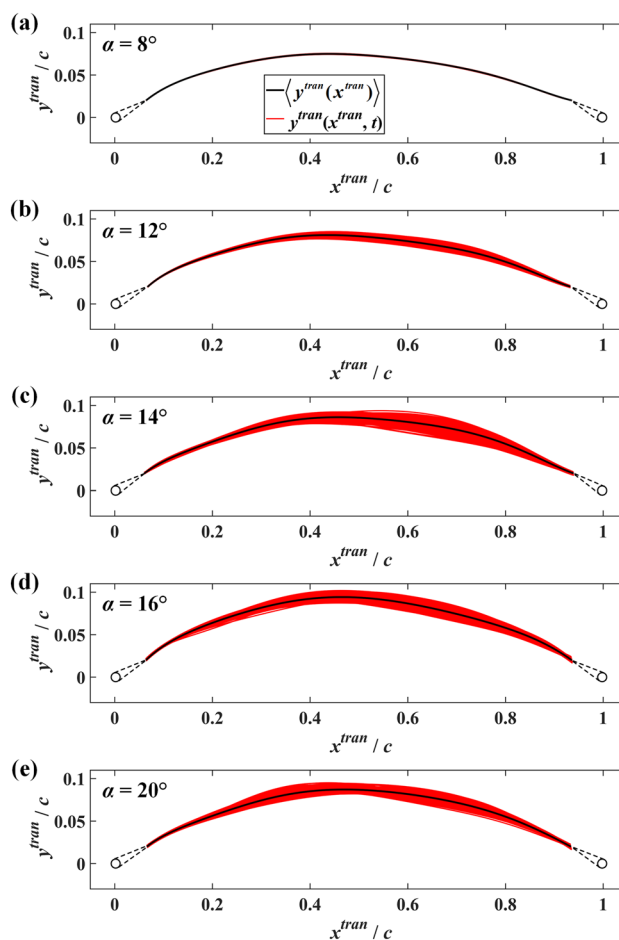

Fig. 3 Superpositions of membrane patterns at different angles of attack. **a** $\alpha = 8°$; **b** $\alpha = 12°$; **c** $\alpha = 14°$; **d** $\alpha = 16°$; **e** $\alpha = 20°$

amplitude increase first and then decrease with the increase in α. When $\alpha = 8°$, the camber of the membrane wing is around 7.5% c, but the vibration amplitude is less than one-tenth of the amplitudes in other higher α cases, which is negligibly small. The membrane patterns almost coincide at all instants, which means that the membrane wing is in the deformed steady state at $\alpha = 8°$. When $\alpha \geq 12°$, the vibration amplitude begins to increase obviously, indicating the dynamic balance state. The mean camber reaches the maximum of around 9.4% c at $\alpha = 16°$, and the vibration amplitude reaches the maximum of around 0.5% c at $\alpha = 14°$. Additionally, the chordwise vibration modes of the membrane wing shown in Fig. 4 vary with the increase in α. The vibration mode gradually transits from the first order at $\alpha = 12°$ and 14° to the second order at $\alpha = 16°$ and 20°.

4 Fluid–structure interaction

PIV data were further analyzed to quantitatively study the influence of α on the fluid–structure interaction of the membrane wing. The statistical characteristics, spectral characteristics and the evolution of instantaneous flow structures around the wing were mainly investigated.

4.1 Statistical characteristics

The nondimensional time-averaged velocity ($\sqrt{\langle U \rangle^2 + \langle V \rangle^2} \big/ U_\infty$) contours at different α are presented in Fig. 5. The red dashed curves denote the positions where the mean streamwise velocity component equals to 0 ($\langle U \rangle = 0$), which represent the scale of the separation region over the upper surface (Munday and Taira 2018). The phase-averaged membrane patterns are superposed. All the membrane vibrations are amplified by a factor of 3 for better display. When $\alpha = 8°$, the flow is totally attached to the upper surface. The membrane is

Fig. 4 Kinematic parameters of the membrane wing. **a** Mean deformations; **b** vibration amplitudes

dominated by mean deformation, which belongs to the DSS region. When $\alpha = 12°$, weak separation occurs near the TE. The membrane enters the DBS region and vibrates at the first-order mode. When α increases to 14° and 16°, the scale of the separation region gradually increases, and the separation point of the mean flow gradually promotes to the location of $x/c \approx 0.8$. When $\alpha = 20°$, the separation point further promotes to $x/c \approx 0.4$, resulting in a large separation region over the upper surface of the wing. The membrane vibrates at the second-order mode. The flow separation of the current membrane wing with the variation of α is consistent with the TE separation of airfoils in low-speed aerodynamics (Polhamus 1996). Besides, it is observed that the location of the separation point is near the antinode where the vibration amplitude is around the maximum.

The distributions of the nondimensional turbulent kinetic energy (TKE, $\langle u'^2 + v'^2 \rangle \big/ U_\infty^2$), which reflects the velocity fluctuation magnitude, are shown in Fig. 6. The convergence of the TKE fields can be ensured by adopting the maximum sampling number of 1.9×10^4 for TKE calculation (see Appendix 1). When $\alpha = 8°$, the velocity fluctuations are very low due to the attached flow and the weak vibration of membrane. When $\alpha = 12°$, high-velocity fluctuations begin to appear near the wing surface because the intensified membrane vibration injects disturbance into the flow field. When $\alpha = 14°$ and 16°, the membrane vibration increases further, injecting stronger disturbance into the flow field. Meanwhile, the scale of the separation region increases, enhancing the unsteadiness of the flow. These two factors lead to the further increase in turbulent kinetic energy over the wing. When $\alpha = 20°$, the separation point is close to the LE. Accordingly, the turbulent kinetic energy is concentrated near the separation point and in the separated shear layer. The velocity fluctuation near the wing surface is relatively weak after the separation point.

4.2 Spectral characteristics

As displayed in Fig. 7, the global frequency spectra of the flow fields and the membrane vibrations at different angles of attack were obtained with Fourier mode decomposition (FMD) proposed by Ma et al. (2015). For a selected sampling region, single-point discrete Fourier transform (DFT) was firstly applied to the original velocity data at every mesh node to get a Fourier mode matrix $\boldsymbol{c}_k$ (Wang et al. 2018; He et al. 2023)

$$\boldsymbol{c}_k = \frac{1}{N} \sum_{n=0}^{N-1} \boldsymbol{F}_n e^{-i\left(\frac{2\pi k}{N}\right)n}, \tag{4}$$
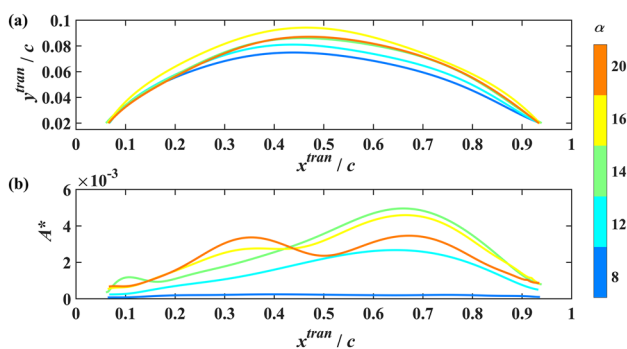
Fig. 5 Time-averaged velocity contours. **a** $\alpha = 8°$; **b** $\alpha = 12°$; **c** $\alpha = 14°$; **d** $\alpha = 16°$; **e** $\alpha = 20°$
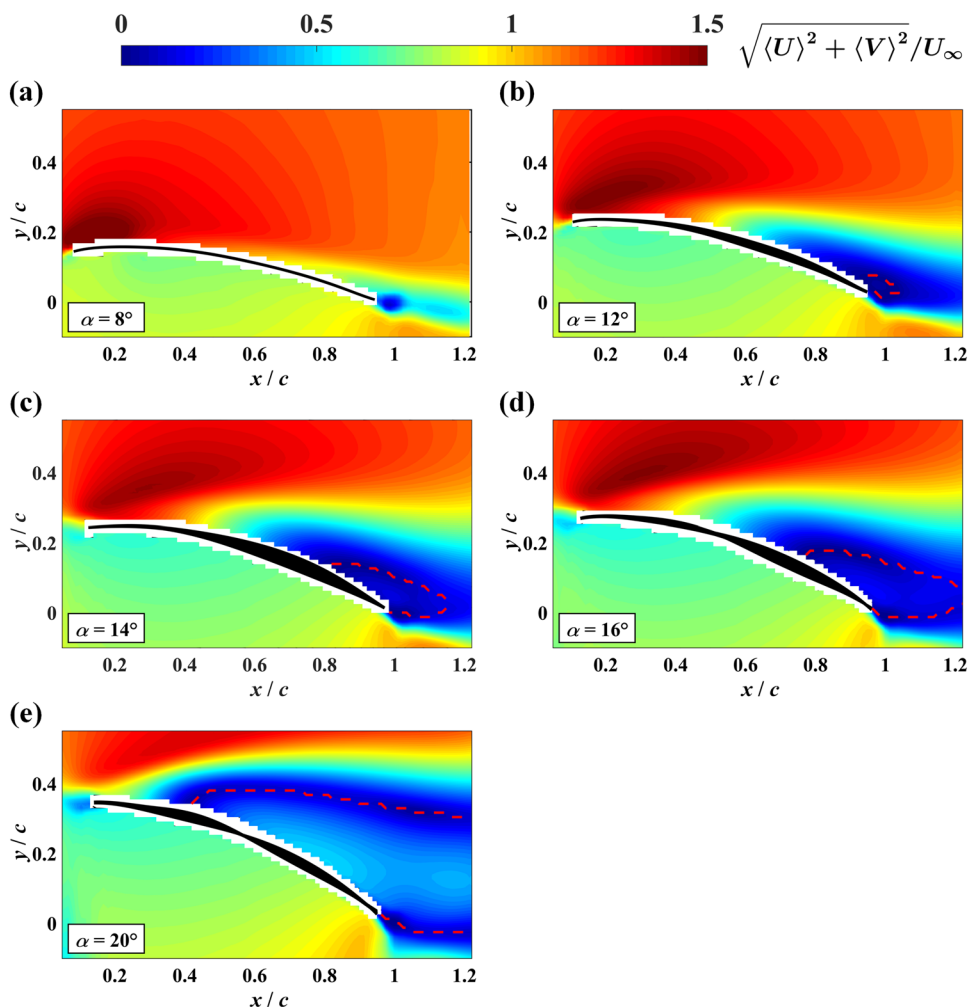

where $N = 1.9 \times 10^4$ is the total sampling number of the image pairs, and $\boldsymbol{F}_n$ is the original velocity complex matrix where the real and imaginary parts are the streamwise and vertical velocities, respectively. The global power spectrum density (PSD_k) was further defined as

$$\text{PSD}_k = \left\| \frac{2N|\boldsymbol{c}_k|^2}{\pi f_s} \right\|, \tag{5}$$

where $\|\cdot\|$ is the Frobenius norm, and f_s is the sampling frequency (1 kHz). The effect of the sampling region on the PSD peaks of FMD is evaluated at different angles of attack in Appendix 2, and the sampling regions in Fig. 6 are finally selected. For the membrane vibrations, DFT of membrane displacements at 200 chordwise equidistant positions was similarly conducted with Eq. (4), and the PSD of global membrane vibrations was then obtained with Eq. (5). Due to the large sampling number, filtering or windowing was not used in this study.

For the membrane vibrations in Fig. 7, the dominant frequencies are 33.2 Hz, 33.5 Hz, 35.1 Hz, 68.1 Hz, 67.2 Hz at $\alpha = 8°$, 12°, 14°, 16°, 20°, respectively. The PSD peak of the dominant frequency at $\alpha = 8°$ is approximately thirty times lower than the peaks at other α, suggesting the vibration is very weak. The vibration frequency is not reflected in the spectrum of the flow field at $\alpha = 8°$, so the fluid–structure coupling is weak. For $\alpha \geq 12°$, the flow fields appear obvious dominant frequencies, which are 8.8 Hz, 9.1 Hz, 9.8 Hz, 67.2 Hz, respectively. However, when $12° \leq \alpha \leq 16°$, the dominant frequencies of the flow field and the membrane are inconsistent, indicating an incomplete coupling state. When $\alpha = 20°$, the dominant frequencies of the flow field and the membrane are consistent, indicating a complete coupling state. The weak, incomplete and complete coupling cases are classified with the dashed boxes in Fig. 7.

Fig. 6 Turbulent kinetic energy distributions. **a** $\alpha=8°$; **b** $\alpha=12°$; **c** $\alpha=14°$; **d** $\alpha=16°$; **e** $\alpha=20°$. The white dashed curves in the figures represent the local TKE peaks. The boxes are the sampling regions for the following spectral analyses
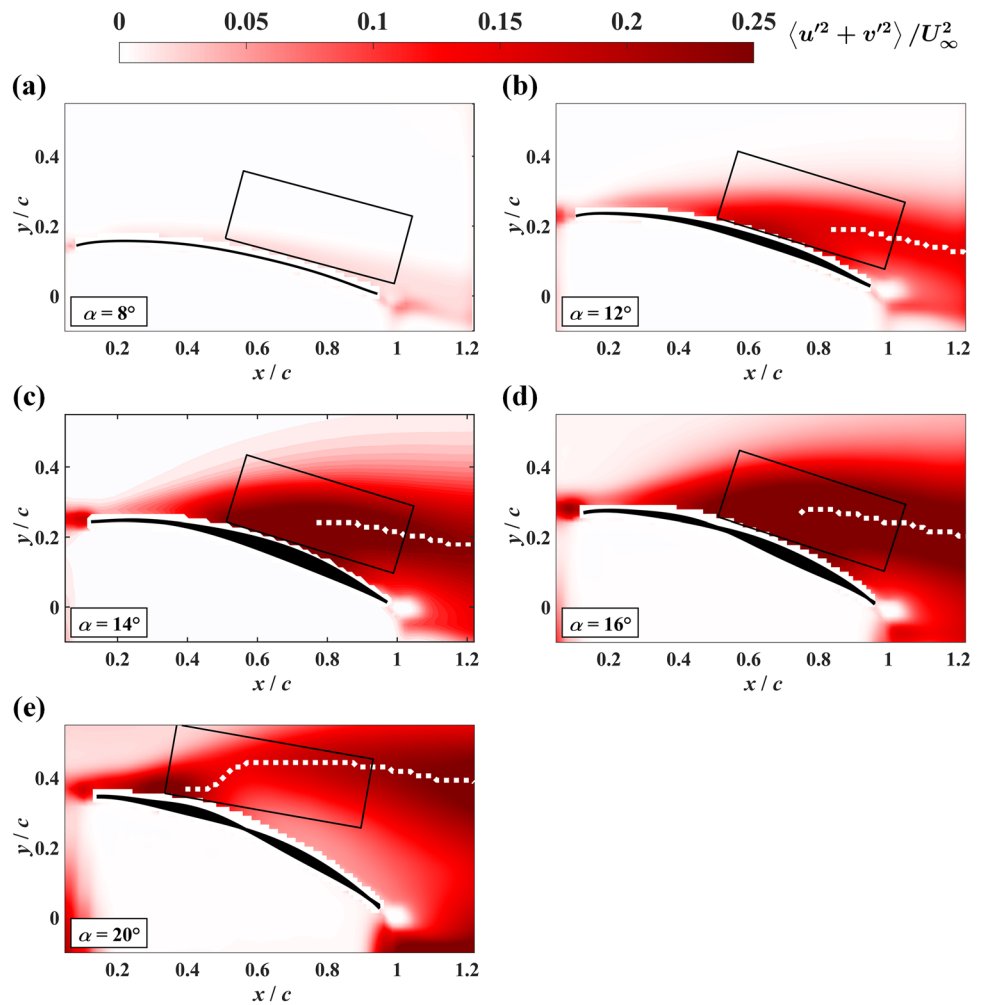
4.3 Evolution of instantaneous flow structures

To explore the mechanisms of the fluid–structure coupling, the evolution of the instantaneous flow structures over the wing surface was studied at $\alpha=8°$ (weak fluid–structure coupling), $\alpha=16°$ (incomplete fluid–structure coupling) and $\alpha=20°$ (complete fluid–structure coupling).

4.3.1 $\alpha=8°$

The root-mean-square (*rms*) distributions of the vertical and the streamwise velocity fluctuations, v_{rms} and u_{rms} are shown in Fig. 8. Due to the attached flow at $\alpha=8°$, both the v_{rms} and the u_{rms} are weak and concentrated over the wing surface. Here, the spectral characteristics of the vertical and the streamwise velocities in the selected region are analyzed separately. The frequency spectra of the velocity signals are also obtained with FMD. As presented in Fig. 9, neither the vertical velocities nor the streamwise velocities have obvious dominant frequencies, let alone the membrane vibration frequency (33.2 Hz) shown in Fig. 7b, indicating

that the flow has not been strongly affected by the weak disturbance of membrane vibration. To display the flow state at $\alpha=8°$, virtual tracers are released from the initial region S1 in Fig. 10. It is found that the flow over the membrane wing just remains attached to the wing surface, presenting quasi-steady characteristics. Therefore, the coupling between the flow and the membrane is weak.

4.3.2 $\alpha=16°$

The *rms* distributions of the velocity fluctuations at $\alpha=16°$ are shown in Fig. 11. The v_{rms} is distributed in the shear layer, while the u_{rms} is mainly concentrated over the wing surface. The frequency spectra of the vertical and the streamwise velocities in the sampling region are shown in Fig. 12. Interestingly, the vertical velocities over the membrane are coupled with the membrane vibration, and their dominant frequencies are 68.1 Hz. However, the lower frequency 9.8 Hz dominates the spectrum of the streamwise velocities. It means the sensitivity of the flow in vertical and streamwise directions is different, and the
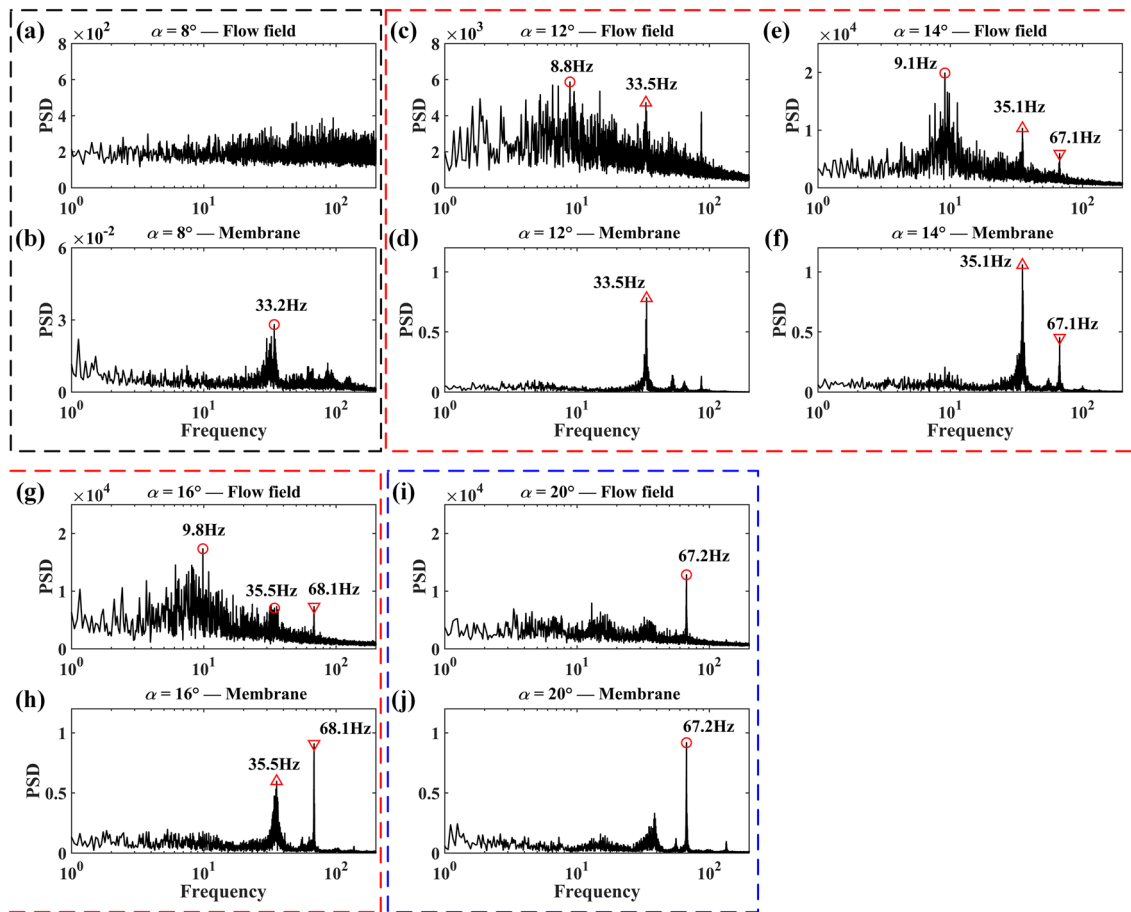
Fig. 7 Global frequency spectra obtained with FMD. **a, c, e, g, i** Spectra of the flow fields; **b, d, f, h, j** spectra of the membrane vibrations. The cases are **a, b** $\alpha = 8°$; **c, d** $\alpha = 12°$; **e, f** $\alpha = 14°$; **g, h** $\alpha = 16°$; **i, j** $\alpha = 20°$. The black, red and blue boxes correspond to the weak, incomplete and complete fluid–structure coupling, respectively
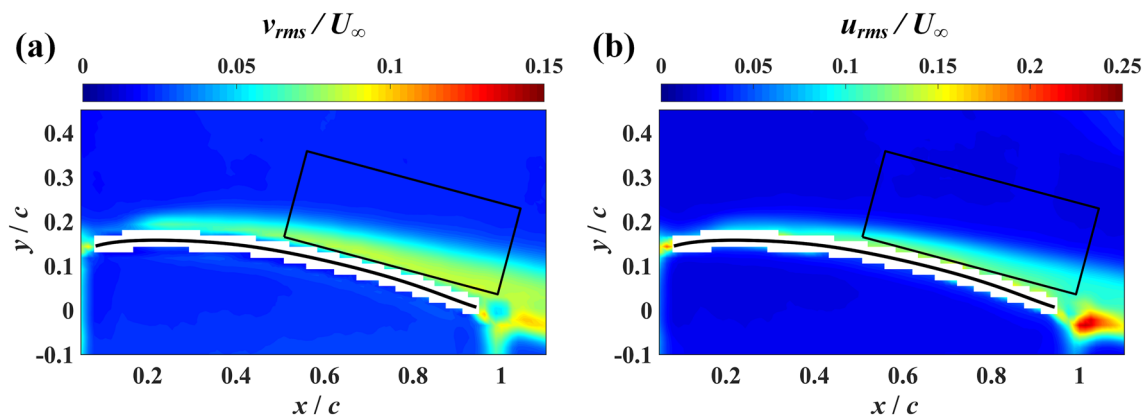

Fig. 8 Distributions of the velocity statistics at $\alpha = 8°$. **a** *rms* of the vertical velocity fluctuations; **b** *rms* of the streamwise velocity fluctuations

vertical velocities over the wing surface are more susceptible to membrane vibration. Consequently, the flow is incompletely coupled with the membrane.

To analyze the mechanism of the incomplete fluid–structure coupling, the velocity signals at the virtual probe P1 in Fig. 11 are firstly investigated. P1 is near the wing surface

Fig. 9 Frequency spectra of the velocities at $\alpha = 8°$. **a** Vertical velocity spectra; **b** streamwise velocity spectra
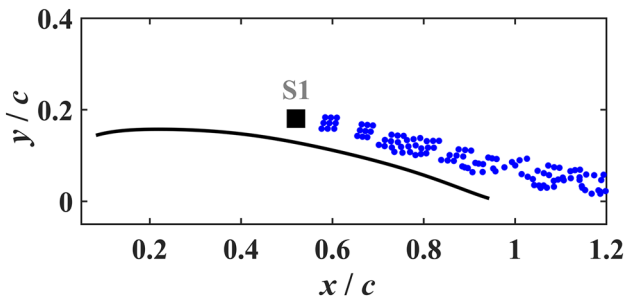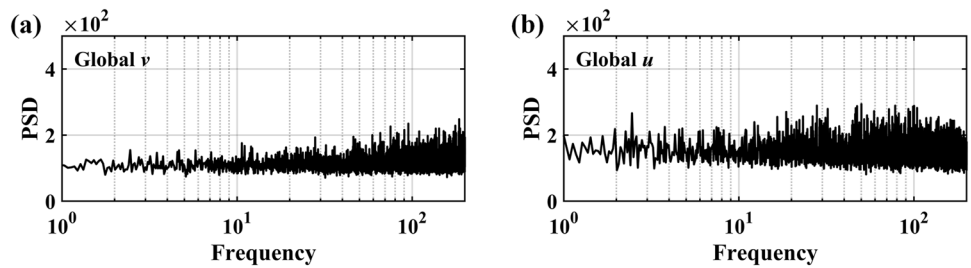

Fig. 10 Exemplary instantaneous flow at $\alpha = 8°$ (displayed by virtual dye visualization)

and located in the u_{rms} concentrated region. The time histories of the streamwise and the vertical velocities at P1 are shown in Fig. 13. $t^* = t \cdot f_{mem\_dom}$ represents the nondimensional time sequence based on the dominant frequency of membrane vibration f_{mem_dom}, which is 68.1 Hz at $\alpha = 16°$.

Similar to He and Wang (2020), the velocity signals are denoised by proper orthogonal decomposition (POD) reconstruction and discrete cosine transform (DCT). As shown, P1−u and P1−v are negatively correlated. When $t^* = 0.41$, 6.74 and 13.62, P1−u reaches the local minima of approximately −0.5 U_∞, indicating the occurrence of strong reverse flows over the wing surface. Meanwhile, P1−v reaches the local maxima, corresponding to the upward movement of the fluid. Additionally, the dominant frequency of the global u is 9.8 Hz in Fig. 12. The corresponding timescale is $\Delta t^* = 68.1/9.8 \approx 7$, which is also the time interval of the strong reverse flows in streamwise direction.

Evolution of the instantaneous flow structures over the membrane wing at $\alpha = 16°$ is further investigated by virtual dye visualization as well as the instantaneous pressure gradients. The virtual tracers are released from two initial regions S1 and S2 (see Fig. 14a), which are near the LE and TE, respectively. The pressure gradients are shown by vectors (see Fig. 14b), and the favorable direction of vectors

Fig. 11 Distributions of the velocity statistics at $\alpha = 16°$. **a** *rms* of the vertical velocity fluctuations; **b** *rms* of the streamwise velocity fluctuations. The local peaks of *rms* values are plotted in dashed curves. The antinode L1 is marked by the green pentagram
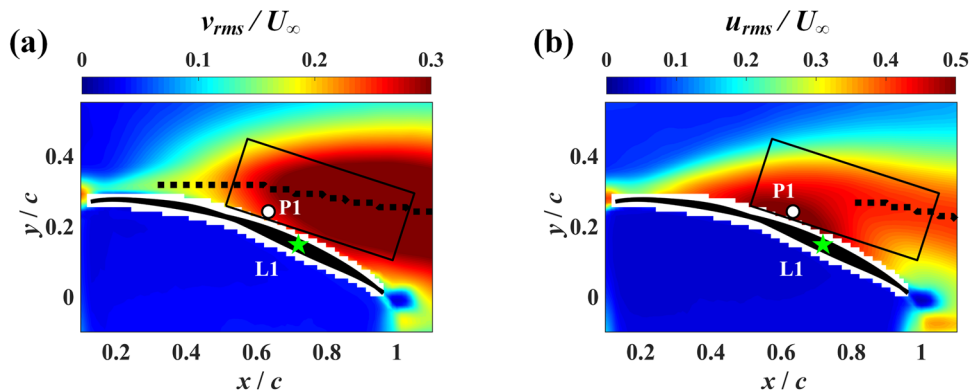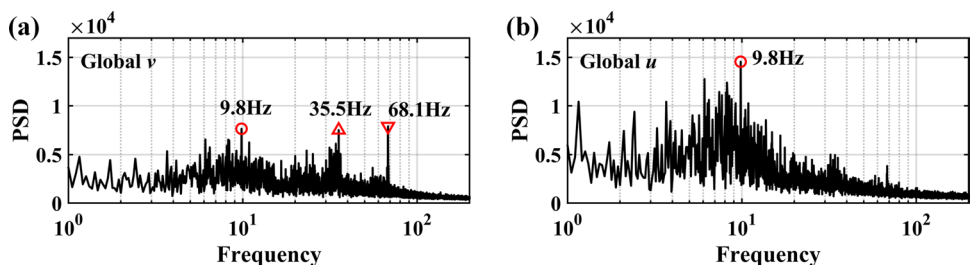

Fig. 12 Frequency spectra of the velocities at $\alpha = 16°$. **a** Vertical velocity spectra; **b** streamwise velocity spectra
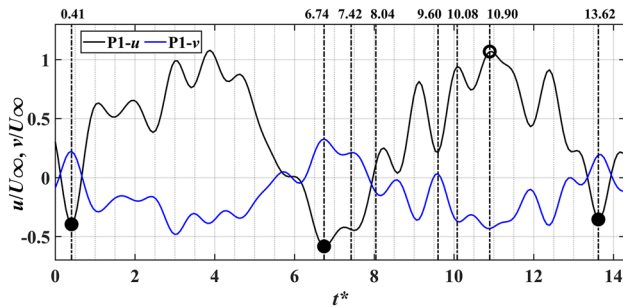
Fig. 13 Time histories of the velocities at P1 at $\alpha = 16°$. P1-u and P1-v are denoted by the black and blue curves, respectively

indicates the increasing direction of pressure. Besides, the vectors are superposed by the swirl strength λ_{ci} fields to show the locations of vortices. The direction of the pressure gradient vector for a vortex is from its center to outside, indicating the low-pressure region in the vortex center and high-pressure region outside the vortex.

Figure 14 shows the flow structures at the three instants ($t* = 6.74$, 7.42 and 8.04) when the TE reverse flow appears over the wing. The interaction between the leading-edge vortex (LEV) and TE reverse flow at $t* = 6.74$ is clearly shown in Fig. 14a. During the interaction, the LEV is uplifted away from the wing surface by the TE reverse flow. After that, the LEV begins to merge with the TE reverse flow at $t* = 7.42$ in Fig. 14c and finally forms a large-scale LEV at $t* = 8.04$ in Fig. 14e.
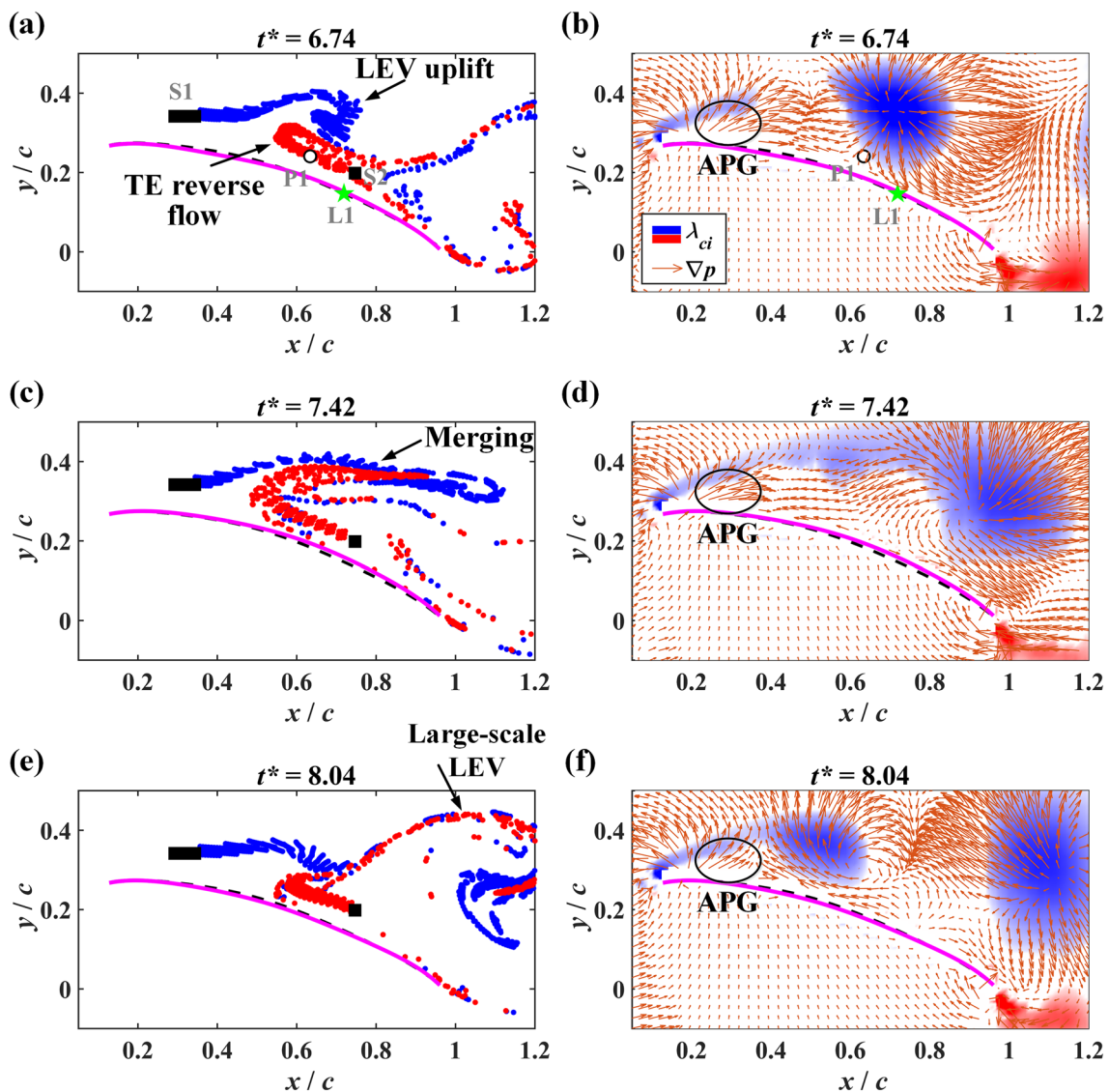

Fig. 14 Evolution of the instantaneous flow structures with the TE reverse flow at $\alpha = 16°$. **a, c, e** Virtual dye visualization; **b, d, f** instantaneous pressure gradients superposed by λ_{ci} fields. The instants are **a, b** $t* = 6.74$; **c, d** $t* = 7.42$; **e, f** $t* = 8.04$

Essentially, Fig. 14 depicts the evolution process when the flow temporarily separates from the wing. A similarity can be found from the pressure gradients in Fig. 14b, d and f that there is always a streamwise adverse pressure gradient (APG) region near the LE. The APG region hinders the downstream convection of the fluid and sharply decelerates the fluid. As a result, the flow tends to separate after the APG region. This is the reason for the temporary flow separation in Fig. 14, and the TE reverse flow is the outcoming of the flow separation.

Moreover, Fig. 15 displays the flow structures at the three instants ($t* = 9.60$, 10.08 and 10.90) without the TE reverse flow. During the downstream convection, the LE flow gradually loses stability and rolls up a small-scale LEV at $t* = 10.08$ in Fig. 15c. After that, the flow will temporarily

attach to the wing surface at $t* = 10.90$ in Fig. 15e. The streamwise velocity at P1 reaches local maximum at the same instant.

From the pressure gradients in Fig. 15b, d and f, a streamwise favorable pressure gradient (FPG) region always exists near the LE, and the APG region is postponed to the downstream. It means that the fluid will be accelerated in the FPG region before entering the APG region. Hence, the fluid has more kinetic energy to overcome APG and suppress flow separation. This is the reason for the temporary flow attachment in Fig. 15.

To sum up, the periodically alternating APG and FPG near the LE of the membrane wing lead to the unsteady flow separation and reattachment, resulting in periodic presence and absence of the TE reverse flow. Accordingly, different
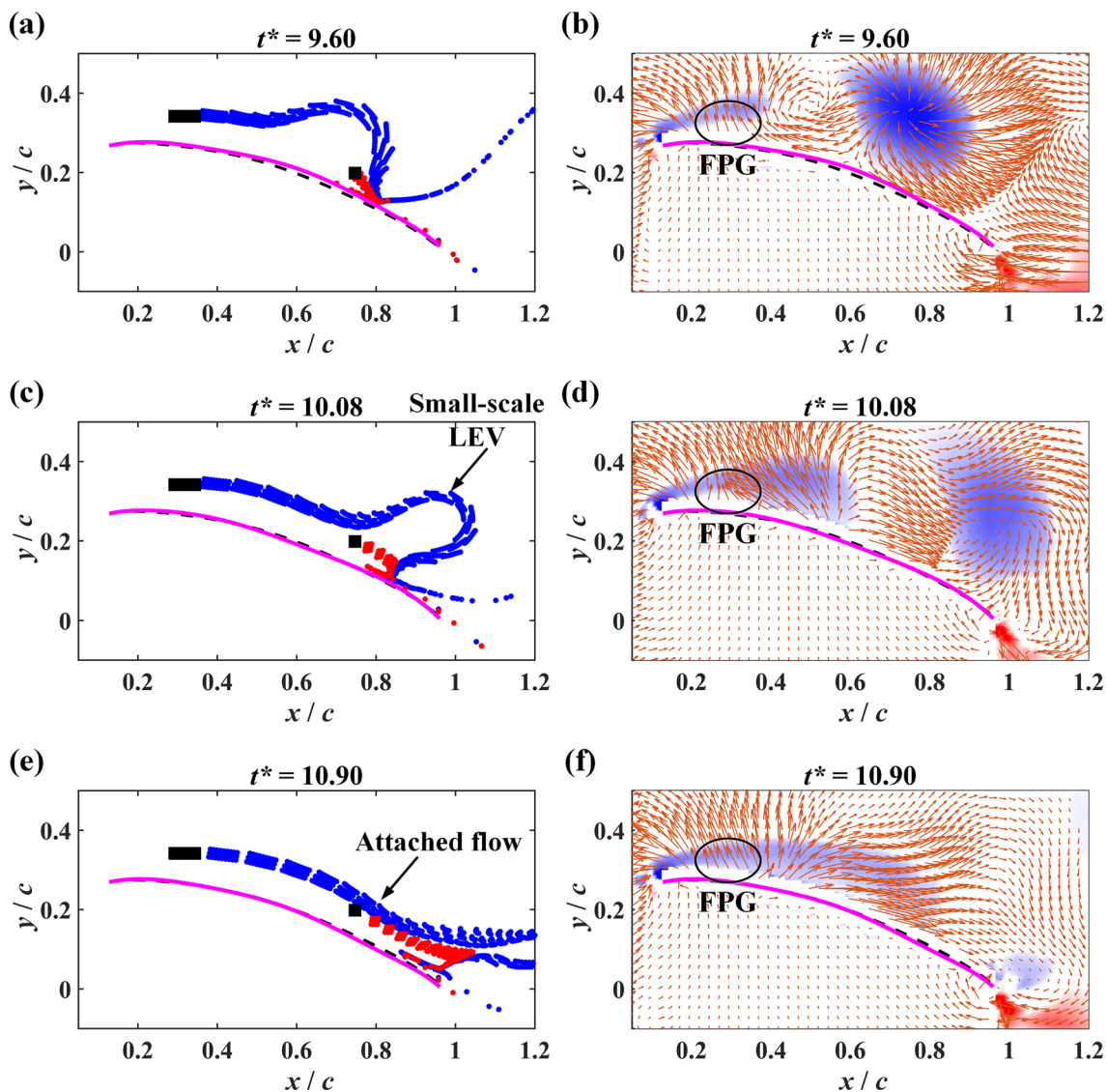

Fig. 15 Evolution of the instantaneous flow structures without the TE reverse flow at $\alpha = 16°$. **a, c, e** Virtual dye visualization; **b, d, f** instantaneous pressure gradients superposed by λ_{ci} fields. The instants are **a, b** $t* = 9.60$; **c, d** $t* = 10.08$; **e, f** $t* = 10.90$

flow regimes occur upon the wing surface, forming LEVs with different scales. These findings above reveal the incomplete fluid–structure coupling mechanism.

For the Reynolds number studied in this paper, it is interesting that the transition from the weak coupling to the incomplete coupling approximately coincides with the transition from the DSS region to the DBS region reported by He et al. (2022). The possible mechanism is discussed here. When $\alpha = 8°$, the flow is not strongly affected by the negligibly small disturbance of membrane vibration and just remains attached to the wing surface. Therefore, the coupling between the flow and the membrane located in the DSS region is weak. With the increase in α, the flow begins to separate temporarily over the membrane surface, leading to the appearance of the streamwise reverse flow. This greatly enhances the unsteadiness of the flow (see the TKE distributions in Fig. 6). According to Li et al. (2022), the unsteadiness of the flow can be reflected by the intensified pressure fluctuations over the membrane surface, which act as an external forcing to drive the membrane to move and vibrate. The forcing frequency coinciding with the natural frequencies of the fluid–structure system will cause certain reinforced vibration modes of the membrane (Serrano-Galiano et al. 2018), which belong to the dynamic balanced state (DBS). In brief, the main reason for the incomplete fluid–structure coupling is the unsteady flow separation and reattachment, which simultaneously increases the unsteadiness of the flow over the membrane wing and probably contributes to the DSS-DBS transition of the membrane. Although the DSS-DBS transition and the incomplete fluid–structure coupling are closely correlated in the current study, their relationship needs to be scrutinized in more cases with different aeroelastic parameters.

4.3.3 $\alpha = 20°$

The *rms* distributions of the velocity fluctuations at $\alpha = 20°$ are illustrated in Fig. 16, in which the v_{rms} is distributed in the separated shear layer, and the u_{rms} is mainly concentrated before the separation point. Similarly, the frequency spectra of the vertical and the streamwise velocities in the sampling region are plotted in Fig. 17. It is seen that 67.2 Hz is the dominant frequency in both the vertical velocity spectra (Fig. 17a) and the streamwise velocity spectra (Fig. 17b), suggesting that the flow evolution is completely coupled with the membrane vibration.

Figure 18 further shows the evolution of the instantaneous flow structures in approximately one vibration cycle at the three instants $t^* = 0$, 0.50 and 1.00 at $\alpha = 20°$. It is seen that the TE reverse flow always exists upon the wing surface due to the large flow separation. Consequently, the LE flow always merges with the TE reverse flow near the separation point to form LEVs. When $t^* = 0$, there is a LEV in the shear layer over the wing. The scale of the LEV gradually increases during the downstream convection. When $t^* = 0.50$, the shear layer is excited by the membrane bulge near the separation point at $x/c \approx 0.4$ and gradually rolls up the next LEV. Due to the low pressure in the LEV center and high pressure outside the LEV, the direction of pressure gradient vector is from the center to outside of the LEV. As a result, the favorable pressure gradients over the wing surface are attributed to the shedding of adjacent LEVs. The

Fig. 16 Distributions of the velocity statistics at $\alpha = 20°$. **a** *rms* of the vertical velocity fluctuations; **b** *rms* of the streamwise velocity fluctuations
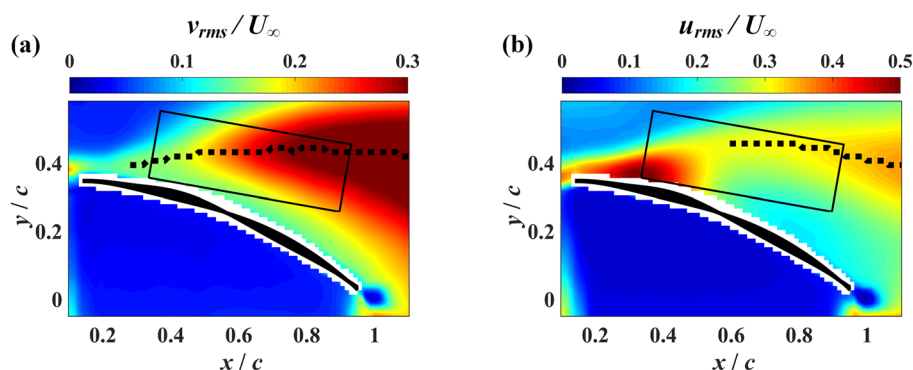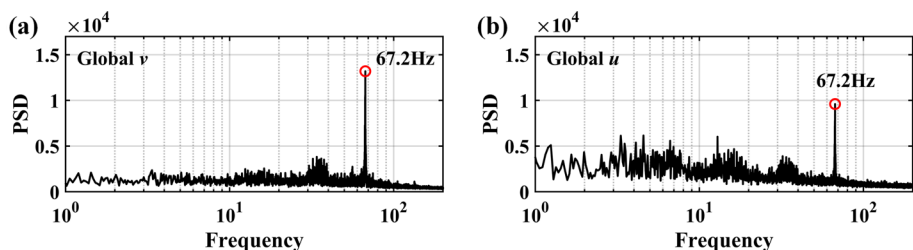

Fig. 17 Frequency spectra of the velocities at $\alpha = 20°$. **a** Vertical velocity spectra; **b** streamwise velocity spectra
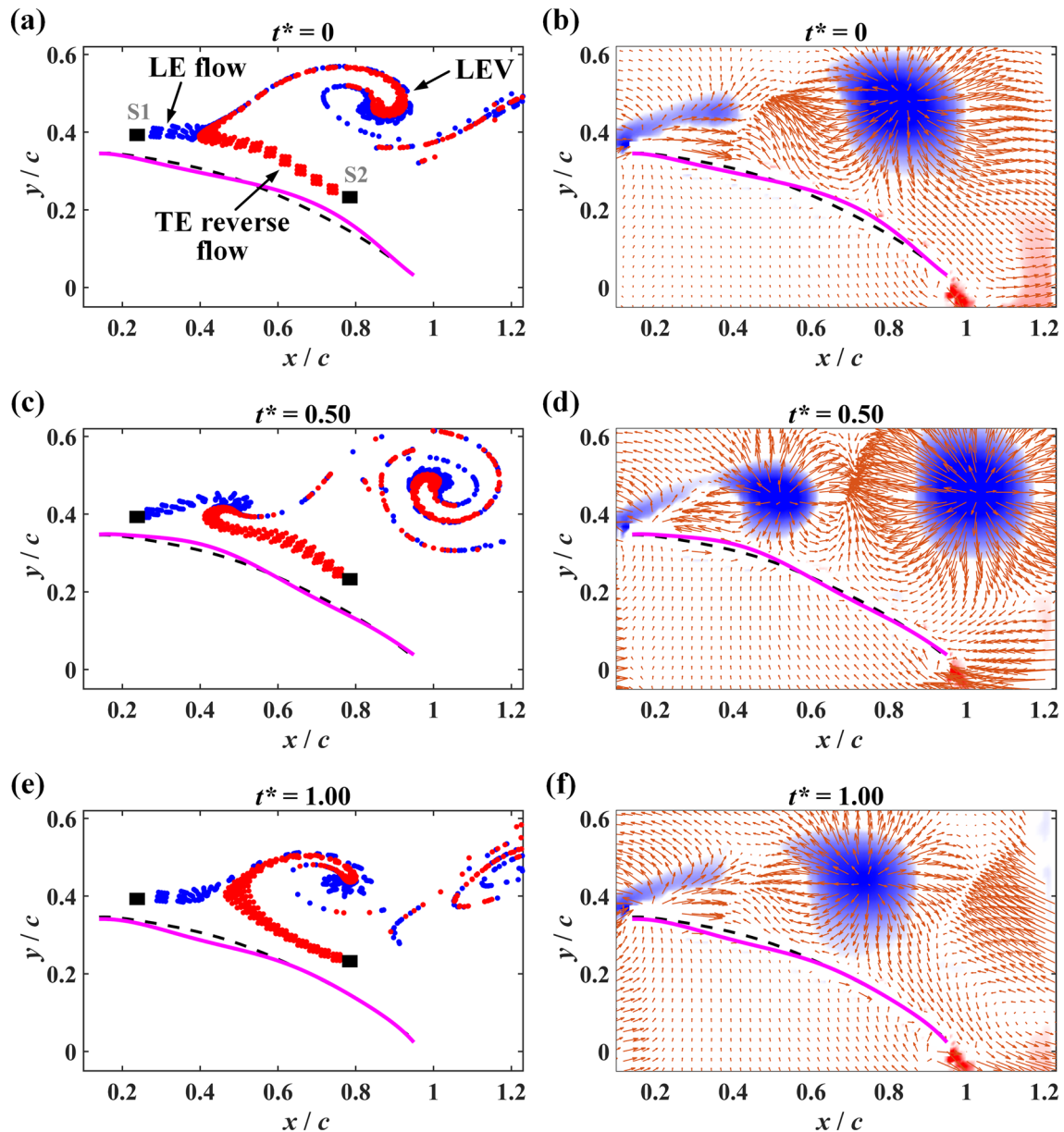
Fig. 18 Evolution of the instantaneous flow structures at $\alpha=20°$. **a, c, e** Virtual dye visualization; **b, d, f** instantaneous pressure gradients superposed by λ_{ci} fields. The instants are **a, b** $t^*=0$; **c, d** $t^*=0.50$; **e, f** $t^*=1.00$

flow structures at $t^*=1.00$ are almost identical with those at $t^*=0$. Therefore, the rolling up of LEVs in the separated shear layer is coupled with membrane vibration, which is the most important feature of fluid–structure coupling at $\alpha=20°$.

5 Conclusions

The flow fields and membrane deformations of a flexible membrane wing at $Re=6\times10^4$ are investigated by the time-resolved synchronous measurements. The influence of

angles of attack on the fluid–structure interaction of membrane wing is studied in the range of $\alpha=8°\sim20°$. The conclusions are as follows.

The coupling state between the flow field and the membrane vibration is related to angles of attack. When $\alpha=8°$, the coupling between the flow and the membrane is weak. Neither the vertical velocities nor the streamwise velocities have obvious dominant frequencies, indicating that the flow has not been strongly affected by the weak disturbance of membrane vibration. When $12\leq\alpha\leq16°$, the vertical velocities over the membrane start to couple with the membrane

vibration, but the streamwise velocities present lower dominant frequencies (~ 9 Hz). The different susceptibility of the flow in vertical and streamwise directions implies that the flow is incompletely coupled with the membrane. When $\alpha = 20°$, the vertical velocities, the streamwise velocities and the membrane have the same dominant frequency, indicating the complete fluid–structure coupling. Therefore, the appearance of incomplete fluid–structure coupling should be at moderate angles of attack.

The mechanism of the incomplete fluid–structure coupling is further revealed by the colored virtual dye visualization and the instantaneous pressure gradients. The periodically alternating adverse and favorable pressure gradients at the location near the leading edge and before the separation point result in the unsteady flow separation and reattachment, which is the main reason for the incomplete fluid–structure coupling at moderate angles of attack. Accordingly, different flow regimes occur upon the wing surface. When the flow separates temporarily, the trailing-edge reverse flow appears and merges with the leading-edge flow, forming large-scale leading-edge vortices. When the flow tends to attach, the trailing-edge reverse flow disappears. The leading-edge flow gradually forms small-scale leading-edge vortices due to the disturbance of membrane vibration. Therefore, the intermittent fluid–fluid interaction between the leading-edge flow and the trailing-edge reverse flow causes the incomplete fluid–structure coupling.

Appendix 1: Effect of sampling number on the convergence of TKE

The effect of sampling number on the convergence of TKE is provided. As shown in Fig. 19, the variation of TKE at three locations (P1, P2 and P3) is evaluated. P1 is consistent with the location in Fig. 11. P2 and P3 are arbitrarily selected

near the downstream region with high TKE. The sampling number in Fig. 19b ranges from 5×10^2 to 1.9×10^4 with an interval of 5×10^2. When the sampling number is less than 6×10^3, the TKE at all locations changes dramatically with the sampling number, indicating the TKE has not converged. However, when the sampling number is more than 6×10^3, the TKE tends to be stable with the increase in sampling number, which means the gradual convergence of the TKE fields. Consequently, we choose the maximum sampling number of 1.9×10^4 for all the cases in this study, and the convergence of TKE fields can be ensured (see Fig. 19).

Appendix 2: Effect of sampling region on the PSD peaks of FMD

Here, the effect of sampling region on the PSD peaks of FMD is studied. Three sampling regions with different size and location are selected. As displayed in Fig. 20, the sizes of the sampling regions 1, 2 and 3 decrease gradually. Regions 1 and 2 surround the entire membrane wing. The inclining region 3, the same as the region in Fig. 6, covers the partial leeward side of the wing. For the velocity fields in regions 1 and 2, the dominant frequency is 33.5 Hz, corresponding to the vibration frequency of the membrane. However, in the smallest region 3, the dominant frequency is around 8.8 Hz. This is because the incomplete fluid–structure coupling just begins at $\alpha = 12°$, and the reverse flow over the membrane is not strong. With the increase in α, the trailing-edge reverse flow becomes strong enough to influence farther, so the lower frequency dominates the spectra in all the regions (see Fig. 21). For $\alpha = 20°$, the relative heights of the peaks also remain unchanged regardless of the sampling region (see Fig. 22). In sum, the PSD peaks at the beginning α of the incomplete fluid–structure coupling ($\alpha = 12°$) are influenced by the sampling region.
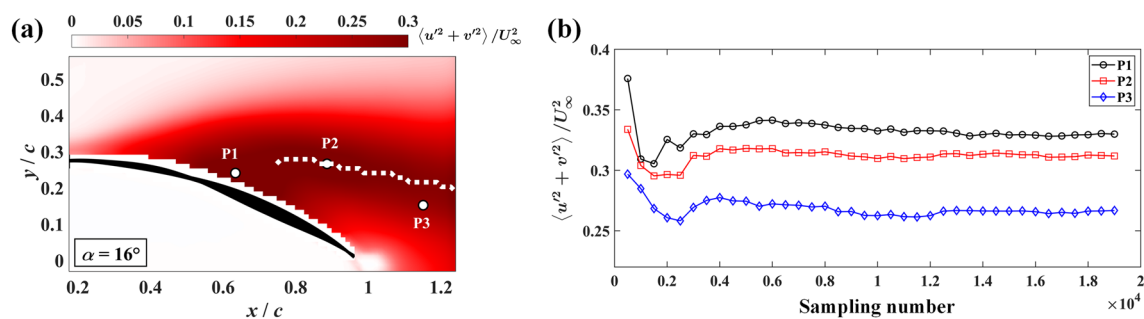

Fig. 19 Effect of sampling number on the convergence of turbulent kinetic energy fields. **a** TKE distributions at $\alpha = 16°$; **b** variation of TKE with the increase in sampling number

Fig. 20 Effect of sampling region on the PSD peaks at $\alpha = 12°$. **a** Sampling regions; **b** spectrum obtained in region 1; **c** spectrum obtained in region 2; **d** spectrum obtained in region 3

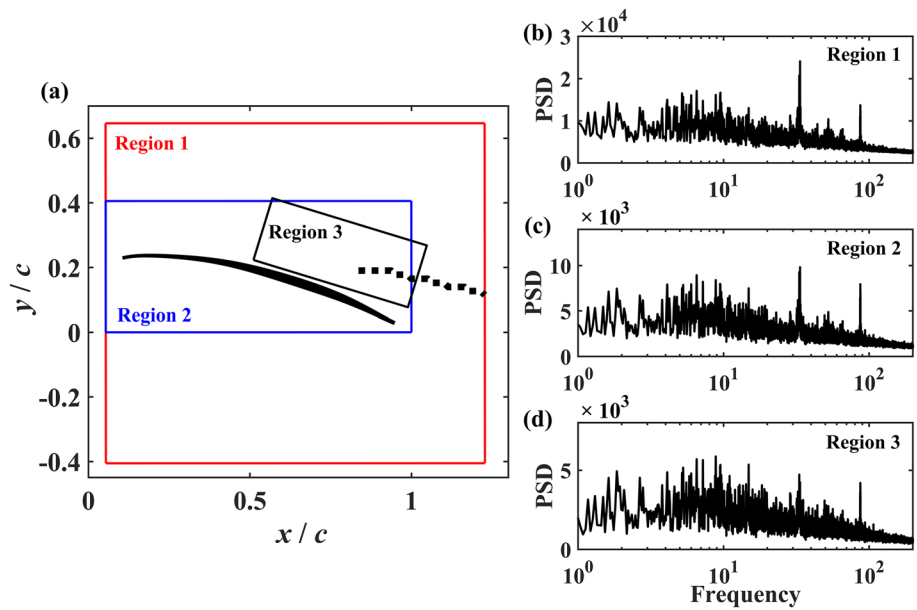**Fig. 21** Effect of sampling region on the PSD peaks at $\alpha = 16°$. **a** Sampling regions; **b** spectrum obtained in region 1; **c** spectrum obtained in region 2; **d** spectrum obtained in region 3
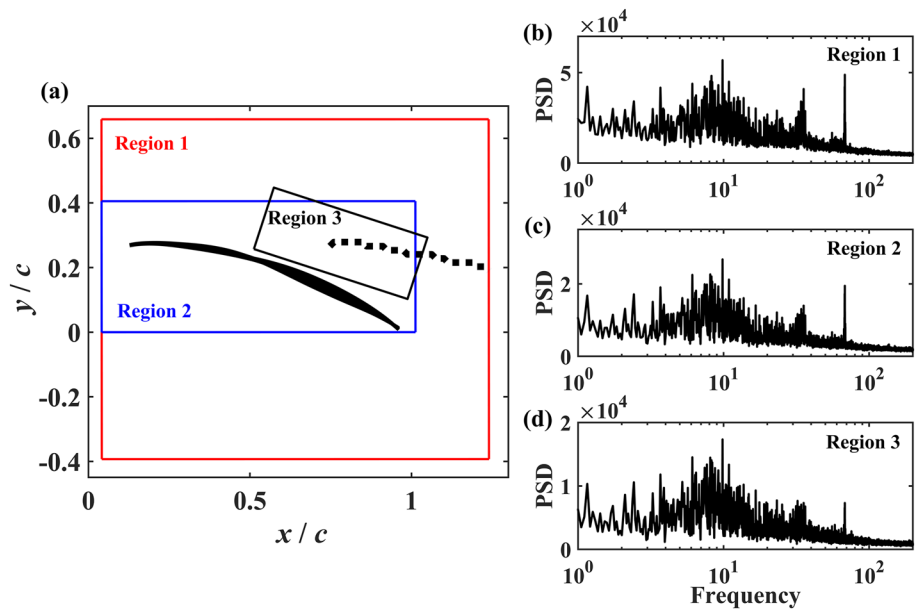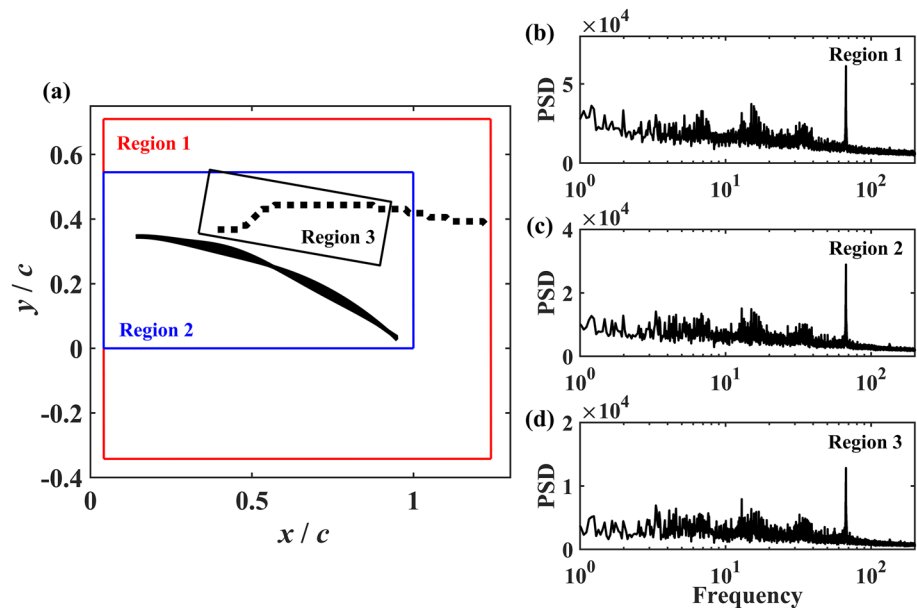
Fig. 22 Effect of sampling region on the PSD peaks at $\alpha = 20°$. **a** Sampling regions; **b** spectrum obtained in region 1; **c** spectrum obtained in region 2; **d** spectrum obtained in region 3

Declarations

Conflict of interests No conflict of interest exists.

Ethical approval This declaration is not applicable.

References

Bleischwitz R, de Kat R, Ganapathisubramani B (2015) Aspect-ratio effects on aeromechanics of membrane wings at moderate Reynolds numbers. AIAA J 53(3):780–788. https://doi.org/10.2514/1.J053522

Bleischwitz R, de Kat R, Ganapathisubramani B (2017) On the fluid-structure interaction of flexible membrane wings for MAVs in and out of ground-effect. J Fluids Struct 70:214–234. https://doi.org/10.1016/j.jfluidstructs.2016.12.001

Champagnat F, Plyer A, Le Besnerais G, Leclaire B, Davoust S, Le Sant Y (2011) Fast and accurate PIV computation using highly parallel iterative correlation maximization. Exp Fluids 50(4):1169–1182. https://doi.org/10.1007/s00348-011-1054-x

Gordnier RE (2009) High fidelity computational simulation of a membrane wing airfoil. J Fluids Struct 25(5):897–917. https://doi.org/10.1016/j.jfluidstructs.2009.03.004

He X, Wang JJ (2020) Fluid-structure interaction of a flexible membrane wing at a fixed angle of attack. Phys Fluids 32:127102. https://doi.org/10.1063/5.0029378

He GS, Pan C, Feng LH, Gao Q, Wang JJ (2016) Evolution of Lagrangian coherent structures in a cylinder-wake disturbed flat plate boundary layer. J Fluid Mech 792:274–306. https://doi.org/10.1017/jfm.2016.81

He GS, Wang JJ, Pan C, Feng LH, Gao Q, Rinoshika A (2017) Vortex dynamics for flow over a circular cylinder in proximity to a wall. J Fluid Mech 812:698–720. https://doi.org/10.1017/jfm.2016.812

He X, Guo QF, Wang JJ (2022) Regularities between kinematic and aerodynamic characteristics of flexible membrane wing. Chin J Aeronaut 35(11):209–218. https://doi.org/10.1016/j.cja.2022.03.015

He X, Guo QF, Xu Y, Feng LH, Wang JJ (2023) Aerodynamics and fluid-structure interaction of an airfoil with actively controlled flexible leeward surface. J Fluid Mech 954:A34. https://doi.org/10.1017/jfm.2022.1017

Hu YW, Feng LH, Wang JJ (2020) Passive oscillations of inverted flags in a uniform flow. J Fluid Mech 884:A32. https://doi.org/10.1017/jfm.2019.937

Huang GJ, Xia YJ, Dai YT, Yang C, Wu Y (2021) Fluid-structure interaction in piezoelectric energy harvesting of a membrane wing. Phys Fluids 33:063610. https://doi.org/10.1063/5.0054425

Jensen A, Pedersen GK, Wood DJ (2003) An experimental study of wave run-up at a steep beach. J Fluid Mech 486:161–188. https://doi.org/10.1017/S0022112003004543

Kline SJ, McClintock FA (1953) Describing uncertainties in single-sample experiments. Mech Eng 75(1):3–8

Li G, Jaiman RK, Khoo BC (2021) Flow-excited membrane instability at moderate Reynolds numbers. J Fluid Mech 929:A40. https://doi.org/10.1017/jfm.2021.872

Li G, Jaiman RK, Khoo BC (2022) Aeroelastic mode decomposition framework and mode selection mechanism in fluid-membrane interaction. J Fluids Struct 108:103428. https://doi.org/10.1016/j.jfluidstructs.2021.103428

Liu X, Katz J (2006) Instantaneous pressure and material acceleration measurements using a four-exposure PIV system. Exp Fluids 41(2):227. https://doi.org/10.1007/s00348-006-0152-7

Ma LQ, Feng LH, Pan C, Gao Q, Wang JJ (2015) Fourier mode decomposition of PIV data. Sci China Technol Sci 58(11):1935–1948. https://doi.org/10.1007/s11431-015-5908-y

Mizoguchi M, Itoh H (2013) Effect of aspect ratio on aerodynamic characteristics at low Reynolds numbers. AIAA J 51(7):1631–1639. https://doi.org/10.2514/1.J051915

Munday PM, Taira K (2018) Effects of wall-normal and angular momentum injections in airfoil separation control. AIAA J 56(5):1830–1842. https://doi.org/10.2514/1.J056303

Pan C, Xue D, Xu Y, Wang JJ, Wei RJ (2015) Evaluating the accuracy performance of Lucas-Kanade algorithm in the circumstance of PIV application. Sci China Phys Mech Astron 58(10):104704. https://doi.org/10.1007/s11433-015-5719-y

Polhamus EC (1996) A survey of Reynolds number and wing geometry effects on lift characteristics in the low speed stall region. NASA CR-4745.

Qu Y, Wang JJ, Feng LH, He X (2019) Effect of excitation frequency on flow characteristics around a square cylinder with synthetic jet positioned at front surface. J Fluid Mech 880:764–798. https://doi.org/10.1017/jfm.2019.703

Rodríguez-López E, Carter DW, Ganapathisubramani B (2021) Dynamic mode decomposition-based reconstructions for fluid-structure interactions: an application to membrane wings. J Fluids Struct 104:103315. https://doi.org/10.1016/j.jfluidstructs.2021.103315

Rojratsirikul P, Wang Z, Gursul I (2009) Unsteady fluid-structure interactions of membrane airfoils at low Reynolds numbers. Exp Fluids 46:859–872. https://doi.org/10.1007/s00348-009-0623-8

Rojratsirikul P, Wang Z, Gursul I (2010) Effect of pre-strain and excess length on unsteady fluid-structure interactions of membrane airfoils. J Fluids Struct 26:359–376. https://doi.org/10.1016/j.jfluidstructs.2010.01.005

Serrano-Galiano S, Sandham ND, Sandberg RD (2018) Fluid-structure coupling mechanism and its aerodynamic effect on membrane aerofoils. J Fluid Mech 848:1127–1156. https://doi.org/10.1017/jfm.2018.398

Shadden SC, Dabiri JO, Marsden JE (2006) Lagrangian analysis of fluid transport in empirical vortex ring flows. Phys Fluids 18:047105. https://doi.org/10.1063/1.2189885

Shadden SC, Katija K, Rosenfeld M, Marsden JE, Dabiri JO (2007) Transport and stirring induced by vortex formation. J Fluid Mech 593:315–331. https://doi.org/10.1017/s0022112007008865

Song A, Tian X, Israeli E, Galvao R, Bishop K, Swartz S, Breuer K (2008) Aeromechanics of membrane wings with implications for animal flight. AIAA J 46(8):2096–2106. https://doi.org/10.2514/1.36694

Tiomkin S, Raveh D, Arieli R (2011) Parametric study of a two-dimensional membrane wing in viscous laminar flow. In: 29th AIAA applied aerodynamics conference, AIAA, p 2011–3023. https://doi.org/10.2514/6.2011-3023.

Tregidgo L, Wang Z, Gursul I (2013) Unsteady fluid-structure interactions of a pitching membrane wing. Aerosp Sci Technol 28(1):79–90. https://doi.org/10.1016/j.ast.2012.10.006

Waldman RM, Breuer KS (2017) Camber and aerodynamic performance of compliant membrane wings. J Fluids Struct 68:390–402. https://doi.org/10.1016/j.jfluidstructs.2016.11.013

Wang JS, Wang JJ (2021) Wake-induced transition in the low-Reynolds-number flow over a multi-element airfoil. J Fluid Mech 915:A28. https://doi.org/10.1017/jfm.2021.20

Wang JS, Feng LH, Wang JJ, Li T (2018) Görtler vortices in low-Reynolds-number flow over multi-element airfoil. J Fluid Mech 835:898–935. https://doi.org/10.1017/jfm.2017.781

Xia YJ, Huang GJ, Dai YT, Yang C, Wu Y (2023) Mode transition in fluid-structure interaction of piezoelectric membrane wings. Phys Fluids 35:023609. https://doi.org/10.1063/5.0139882